www.advenergymat.de

Magnesium Substitution in Ni-Rich NMC Layered **Cathodes for High-Energy Lithium Ion Batteries**

Aurora Gomez-Martin,* Friederike Reissig, Lars Frankenstein, Marcel Heidbüchel, Martin Winter, Tobias Placke, and Richard Schmuch*

Ni-rich LiNi_{1-x-v}Mn_xCo_vO₂ (NMC) layered oxides are promising cathode materials for high-energy density lithium ion batteries but suffer from severe capacity fading upon cycling. Elemental substitution (= doping) with Mg has repeatedly attracted attention in NMC materials to overcome instability problems at reasonable cost, yet rational compositional tuning is needed to guarantee sufficient cycle life without compromising energy density on the material level. Herein, a series of Mg-substituted NMC materials with 90 mol% Ni are investigated regarding key performance metrics in NMC || graphite full-cells benchmarked against LiNi_{0.80}Mn_{0.10}Co_{0.10}O₂ and LiNi_{0.90}Mn_{0.05}Co_{0.05}O₂ synthetized using the same co-precipitation route. A linear correlation between cycle life and attainable gravimetric capacities is demonstrated, which are directly influenced by the degree of Mg substitution and the amount of Li+ cycled upon (de-)lithiation processes. A Mg content <2 mol% should be considered to take notable benefit from the increase in Ni content from 80 to 90 mol% to achieve a higher energy density. The present study highlights the importance of evaluating the true implications of elemental substitution on cell performance and is expected to be an insightful guideline for the future development of NMCtype cathode materials in particular with high Ni and low Co content.

1. Introduction

Lithium-ion batteries (LIBs) are the state-of-the-art energy storage technology for portable electronic devices and leading candidates for electric vehicles (EVs) due to their combination of high energy and power density, high energy efficiency, long cycle life, and high safety.^[1] However, the specific energy/

A. Gomez-Martin, L. Frankenstein, M. Heidbüchel, M. Winter, T. Placke, R. Schmuch University of Münster MEET Battery Research Center Institute of Physical Chemistry Corrensstraße 46, 48149 Münster, Germany E-mail: agomezma@uni-muenster.de; richard.schmuch@uni-muenster.de F. Reissig, M. Winter Helmholtz-Institute Münster Forschungszentrum Iülich GmbH Corrensstraße 46, 48149 Münster, Germany

The ORCID identification number(s) for the author(s) of this article can be found under https://doi.org/10.1002/aenm.202103045.

© 2022 The Authors. Advanced Energy Materials published by Wiley-VCH GmbH. This is an open access article under the terms of the Creative Commons Attribution License, which permits use, distribution and reproduction in any medium, provided the original work is properly cited.

DOI: 10.1002/aenm.202103045

energy density of LIBs need to be further improved (>350 Wh kg^{-1} and >750 Wh L^{-1} at cell level) to fully meet the required targets for electro-mobility applications.[1b,2] The development of advanced LIB active materials, with higher specific and volumetric capacities and lower processing costs, is believed to be the most straightforward way to achieve the targets for energy density and costs of future LIBs, and thus to better meet customer needs.

Since the first commercialization of LIBs, the positive electrode (cathode) is regarded as the major bottleneck for further increasing the specific energy of LIBs. Ni-rich $\text{LiNi}_{1-x-y}\text{Mn}_x\text{Co}_y\text{O}_2$ (NMC) and LiNi_{1-x-v}Co_xAl_vO₂ (NCA) layered transition metal (TM) oxides are highly promising cathode materials for EVs due to their highest level of technological maturity combined with high energy density on material level.[3] Extensive research in both the industry and academia has been continually pushing the increase in the Ni

content on both NMC and NCA beyond >80%, while reducing Co content, to further boost the energy density and reduce raw material cost. However, the increase of the Ni content in NMC-type cathode materials inevitably results in a more complex synthesis and several structural instability issues limiting cell cycle life and safety, that is, high reactivity toward moisture (upon storage, processing, and operation), lower thermal stability of the charged electrode, Li+/Ni2+ cation mixing, phase transformation from layered to inactive rock salt NiO phase, micro-crack formation upon cycling, as well as dissolution of TMs from NMC and subsequent deposition at the negative electrode (anode).[4]

One popular and easy to scale-up approach to mitigate instability issues on Ni-rich layered oxides consists of the partial elemental substitution (frequently called "doping") of TMs with alternative cations. Many different cationic substituents (e.g., Al, [5] Mg, [6] Ti, [7] W, [8] Zr, [9] Ta, [10] etc.)—often referred to as dopants-have proven to benefit the cycle life at relatively low amounts (<2 mol%). However, there is a lack of widely accepted theories when it comes to substituting element selection and recent publications are mostly based on trial-and-error by exploring a wide range of possible elements. [2a] For a large-scale application of cathode materials, several considerations should therefore not be overlooked. On the one hand, the incorporation of certain substituents, such as Ti, Al, and Zr, complicates



www.advenergymat.de

the synthesis of the hydroxide/carbonate precursors during co-precipitation, and these are therefore typically introduced through a post-wet sol gel process, followed by diffusion to the bulk during the calcination process at high temperatures (e.g., 600–800 $^{\circ}$ C).[2a,5,9,11] Besides the additional cost of the needed extra synthesis step, the incorporation during calcination can result in compositional inhomogeneity, poor reproducibility, and phase segregation to the surface in some cases. [8a,12] On the other hand, the benefits in cycle life brought by different dopants typically comes at the expense of a sharp decrease in specific capacity, and thus in the energy density on material level.[13] There is some debate as to whether the choice of substituent used really matters, or whether the enhanced performance is just a result of the limited degree of de-lithiation of the material caused by the substituent at a certain operating voltage window.^[4b,14] Even so, the use of substituents still seems one of the most viable strategies to allow the increase of the Ni content in Ni-rich NMC-type layered oxides, while decreasing the content of critical raw materials such as Co. Because of the strongly fluctuating cost of Co due to its limited and geographically concentrated supply and raising moral and environmental concerns due to Co mining, the development of Ni-rich Co-low/Co-free cathode materials is of utmost importance and is currently one of the most pursued topics within the battery community.[15]

Mg has repeatedly attracted significant attention as primary alternative substituent for layered oxide cathodes due to its ease of incorporation through a hydroxide co-precipitation synthesis (i.e., similar solubility product constant, K_{sp} , of Mg $(OH)_2 (K_{sp} 5.61 \times 10^{-12})$ and Ni $(OH)_2 (K_{sp} = 5.5 \times 10^{-15}))$, low cost and abundance. Previous studies on $\tilde{\text{LiCoO}}_2$, [16] NMC, [6b,17] NCA,^[18] and pure LiNiO₂^[6a,12b,13,18a,19] have extensively proven the high effectivity of Mg to improve cycle life, stabilize impedance, and improve thermal stability in relatively small amounts (<5 mol%). Due to the similar ionic radii $(r_{Li}^+ = 0.76 \text{ Å},$ $r_{\rm Mg}^{2+}$ = 0.72 Å), it is believed that Mg²⁺ ions are likely to occupy the lithium layer and act as "pillars", particularly when the substituent content is less than 2 mol%.[19a] The pillar effect caused by electrochemically inactive Mg²⁺ ions can suppress phase transitions and alleviate anisotropic lattice distortion and structure collapse upon (de-)lithiation processes.[19b] However, introducing 5 mol% of Mg into LiNiO2 decreased the capacity by 50 mAh g⁻¹.[13] Interestingly, there is a lack of systematic investigations of the impact of Mg addition in NMC materials on key performance indicators in realistic graphite-based full-cells under practical testing conditions. The evaluation of not only the advantages of elemental substitution by inactive dopants in terms of prolonging cycle life, but also the detrimental effects on other performance metrics, such as specific energy and energy density, is of utmost relevance for the practical development of Ni-rich layered cathode materials.

In this work, Ni-rich Mg-substituted NMC-type cathode materials, LiNi $_{0.90}$ Mn $_{0.05-x}$ Co $_{0.05}$ Mg $_x$ O $_2$ (x=0, 0.010, 0.015, and 0.020) and LiNi $_{0.90}$ Mn $_{0.05}$ Co $_{0.05-x}$ Mg $_x$ O $_2$ (x=0.010), were systematically investigated with regards to electrochemical properties in NCM \parallel graphite full-cells. A fixed Ni content of 90 mol% was considered for all materials, while the Mg content ranged between 1 and 2 mol%. First, the Mg substituent was incorporated into the NMC double hydroxide precursors

through a co-precipitation process using a continuous Couette-Taylor Flow Reactor (CTFR). The CTFR has recently emerged as a novel technology of high relevance for the continuous large-scale production of cathode precursors with desired particle characteristics.^[20] It offers several advantages over established continuous stirred-tank reactor (CSTR) and batch processes, for example, very homogeneous micro-mixing of reactants with higher mixing intensity, drastically reduced processing times and design of dense particles by fast reaction kinetics.[21] Second, the synthesized lithiated layered cathode materials were comprehensively investigated in regard to their particle size and morphology, crystallinity, tap density, and specific surface area, which are highly relevant parameters for practical applications to achieve a high energy density/specific energy on material level. Then, the rate capabilities and longterm cycle life were thoroughly evaluated in NMC || Li metal and NMC || graphite full-cells with regards of the Mg content, respectively. Finally, ex situ X-ray diffraction (XRD) investigations were performed to the de-lithiated Mg-substituted cathode materials after charging to the same upper cut-off voltage and same degree of lithium extraction ratio to shed light onto the long-term stability, unit cell volume changes and thus extent of micro-crack formation upon cycling with regards to Mg content.

2. Results and Discussion

2.1. Morphological and Structural Characterization of Mg-Substituted Ni-Rich NMC Materials

Mg-substituted Ni-rich NMC hydroxide precursors with varying Mg content, Ni_{0.90}Mn_{0.05-x}Co_{0.05}Mg_x(OH)₂ (x=0, 0.010, 0.015, 0.020), and Ni_{0.90}Mn_{0.05}Co_{0.05-x}Mg_x(OH)₂ (x=0.010), were synthesized via a co-precipitation process using a continuous CTFR and identical experimental conditions. The degree of substitution with electrochemically inactive Mg²⁺ was limited to only 1–2 mol% to avoid largely sacrificing the attainable specific capacities. Therefore, when the content of the also inactive Mn⁴⁺ was decreased, a Mg²⁺ amount between 1 and 2 mol% was investigated, but when the content of electrochemically active Co³⁺ was decreased, the degree of substitution with Mg²⁺ was limited to only 1 mol%.

Table 1 lists all synthesized cathode materials with 90 mol% Ni and detailed compositional and microstructural parameters. Figure 1a-e and Figure 1f-j show representative scanning electron microscopy (SEM) images of as-synthetized hydroxide precursors and lithiated materials, respectively. All precursor materials exhibit relatively large spherical secondary particles in the micron-sized range (≈10-13 µm) with a smooth outer surface formed by the agglomeration of nanosized plate-like individual crystals stacked on the (001) face, typical of hydroxide precursors co-precipitated using a CFTR reactor.[21c] However, smaller spherical secondary particles (<10 µm) are present as well. The increase in the Mg content up to 2 mol% seems to promote the agglomeration of Ni-rich hydroxide crystals resulting in slightly denser particles. After calcination, the overall morphology of the secondary particles is preserved, being composed of ≈50-200 nm granular primary particles.

Table 1. Detailed compositional and structural parameters of all synthesized lithiated Ni-rich NMC-type cathode materials.

Targeted stoichiometry	Material	Tap density [g cm ⁻³]	Surface area [m ² g ⁻¹]	d ₅₀ [μm]	d ₉₀ [μm]	d _{mean} [μm]	Measured stoichiometry
LiNi _{0.80} Mn _{0.10} Co _{0.10} O ₂	NMC 801010	2.00 ± 0.15	0.60	12.5 ± 0.8	21.3 ± 1.3	13.0 ± 0.7	LiNi _{0.80} Mn _{0.10} Co _{0.10} O ₂
$LiNi_{0.90}Mn_{0.05}Co_{0.05}O_{2} \\$	NMC 900505	2.02 ± 0.08	0.50	12.9 ± 0.1	20.4 ± 0.7	13.3 ± 0.1	$LiNi_{0.900}Mn_{0.051}Co_{0.049}O_{2}$
$LiNi_{0.90}Mn_{0.04}Co_{0.05}Mg_{0.01}O_{2}$	NMCMg 90040501	2.10 ± 0.10	0.61	12.3 ± 0.3	21.7 ± 0.4	13.2 ± 0.2	$\begin{array}{c} \text{LiNi}_{0.894}\text{Mn}_{0.044}\text{Co}_{0.052}\text{Mg} \\ \\ \text{0.010}\text{O}_{2} \end{array}$
$LiNi_{0.90}Mn_{0.035}Co_{0.050}Mg_{0.015}O_{2} \\$	NMCMg 9003.50501.5	1.95 ± 0.08	0.48	12.7 ± 0.6	20.4 ± 0.7	13.1 ± 0.4	$\begin{array}{c} \text{LiNi}_{0.888} \text{Mn}_{0.036} \text{Co}_{0.059} \text{Mg} \\ \\ \text{0.017} \text{O}_{2} \end{array}$
${\rm LiNi_{0.90}Mn_{0.03}Co_{0.05}Mg_{0.02}O_{2}}$	NMCMg 90030502	2.06 ± 0.03	0.68	12.2 ± 0.8	20.5 ± 1.3	12.6 ± 0.7	$\begin{array}{c} LiNi_{0.899}Mn_{0.028}Co_{0.050}Mg\\ \\ 0.023}O_{2} \end{array}$
$LiNi_{0.90}Mn_{0.05}Co_{0.04}Mg_{0.01}O_{2}$	NMCMg 90050401	2.04 ± 0.05	0.60	12.7 ± 0.5	22.9 ± 1.1	13.9 ± 0.6	$LiNi_{0.891}Mn_{0.057}Co_{0.042}Mg$ $_{0.010}O_{2}$

Further high-magnification SEM micrographs of the lithiated materials, shown in Figure S1, Supporting Information, give evidence of non-significant changes in the shape and size of primary particles with increasing Mg content. Cross-sectional SEM images and energy dispersive X-ray spectroscopy (EDX) analysis shown in Figure 1k-o reveal a dense particle core with

low porosity and a homogeneous distribution of Ni, Co, Mn, Mg within secondary particles. However, as the Mg content lies below the detection limit of the EDX, it was not possible to detect accurately the evolution of the atomic distribution within secondary particles. Inductively coupled plasma-optical emission spectrometry (ICP-OES) analyses confirm only a small

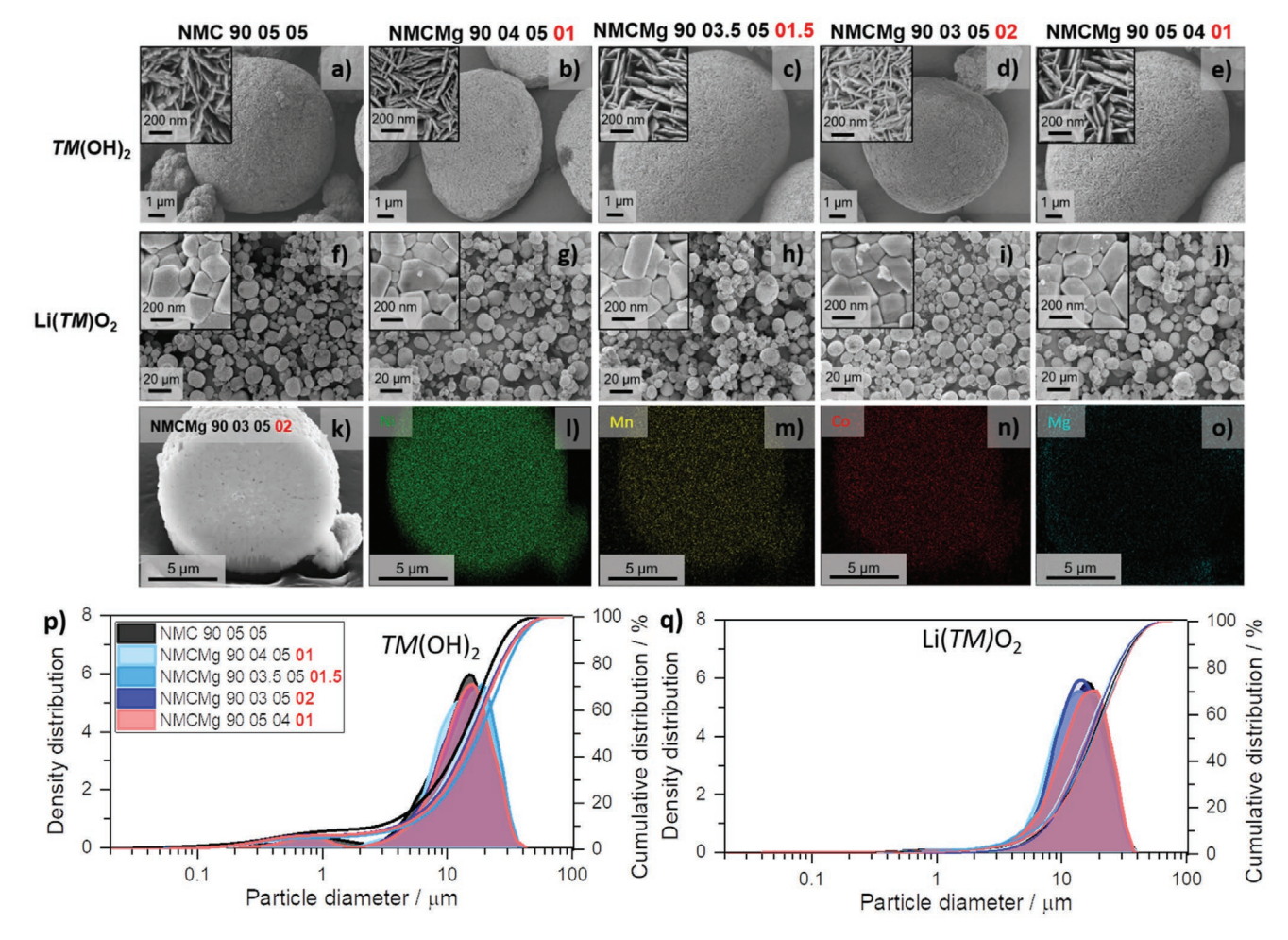


Figure 1. SEM micrographs of hydroxide-based precursors (TM(OH)₂) and lithiated products (LiTMO₂): a, f) NMC900505, b, g) NMCMg 90040501, c, h) NMCMg 9003.50501.5, d, i) NMCMg 90030502, e, j) NMCMg 90050401. TM stands for transition metal. High-magnification SEM micrographs shown in the inset of the figures reveal shape and size of primary particles. EDX elemental mappings of k) NMCMg 90030502 powdered sample corresponding to l) Ni, m) Mn, n) Co, and o) Mg. PSD (by volume) of p) co-precipitated hydroxide precursors and q) lithiated products.





www.advenergymat.de

deviation in composition from their relative targeted stoichiometries (Table 1).

All materials were investigated by laser diffraction to determine the particle size distribution (PSD) of the different coprecipitated hydroxide precursors and lithiated products. Figure 1p,q show the PSD and Table 1 gives a comparison of d_{50} and d_{90} values for all Ni-rich lithiated layered oxide cathodes. As can be seen, the PSDs of most precursor materials are relatively narrow and bimodal. Approximately 50% of the overall particle volume is ≤11-13 µm (see Table S1, Supporting Information, for detailed PSD of hydroxide precursors), whereas d_{90} values are within the range of $\approx 18-22 \mu m$, respectively. The PSDs of the lithiated cathode materials after the calcination are generally shifted to slightly higher values in comparison to the hydroxide precursors. Upon high-temperature calcination, the smaller particles agglomerate to create larger ones, and, therefore, flatten the curves in the range <2 µm, resulting in monomodal particle size distributions. Tap densities in the ≈1.8–2.2 g cm⁻³ range and specific surface areas <0.7 m² g⁻¹ were achieved for the lithiated materials, which are reasonable values for practical applications to reach high areal electrode capacities and reduce parasitic side reactions in contact with the electrolyte.[1b] No clear trends on tap densities and specific surface areas with regards to the Mg content in NMC materials are observed. SEM and PSD analysis of NMC 801010 are also included in the Supporting Information (Figure S2 and Table S1, Supporting Information), confirming similar morphology of secondary particles and PSD in comparison to lithiated products containing 90 mol% Ni. High-energy LIB cells require fabrication of composite electrodes with high areal capacities and high pressed electrode densities, which can be achieved by using cathode materials with high crystallographic density (>4 g cm⁻³), large particle size (≥10 µm), and bimodal size distribution. The good reproducibility of the CFTR reactor facilitates a fair comparison of the electrochemical properties and the individual impact of the degree of Mg substitution on cycle life.

Figure 2a shows the XRD patterns and Rietveld refinements of the synthetized Ni-rich cathode materials. Rietveld refinements were performed to investigate the crystallographic changes with increasing Mg substituent content. Detailed information of refinements, lattice parameters, and cation mixing data can be found in Table S2 and Figure S3, Supporting Information. All patterns can be indexed to a singlephase well-defined hexagonal α-NaFeO₂ structure belonging to the space group $R\overline{3}$ m (PDF 04-013-4377), with little effect from Mg incorporation. The clear splitting of (006)/(102) and (108)/(110) reflections indicates a good hexagonal symmetry within the structure.^[22] Figure 2b shows the evolution of lattice parameters (a and c) as obtained from the Rietveld refinements as a function of the Mg content. In general, a good fit (GOF < 2%) between calculated and experimental XRD patterns could be obtained, suggesting that the refinements are reliable. Calculated values of lattice parameters are consistent with previous works. [19a] Nonetheless, a better goodness of fit with the experimental data (Figure S4a, Supporting Information) was generally achieved when Mg²⁺ was considered to sit in the lithium slab (3a sites) as schematically illustrated in Figure 2c, in agreement with previous experimental results.^[19a] Following the Rietveld results, one could also use the following alternative notation: $[\mathrm{Li}_{1-x}\mathrm{Mg}_x]_{3a}[\mathrm{NiMnCoLi}_x]_{3b}[\mathrm{O}_2]_{6c}$ to describe the Mg placement into the NMC structure when the substituted Li of the Li layer migrate to the TM slab. However, for ease of understanding, Mg-substituted NMC cathodes will be further referred to as "NMCMg" materials followed by the targeted stoichiometries.

A higher Co content typically results in a contraction of the lattice parameters c and a and an increase in the c/a ratio, while higher Mn contents result in a decrease in a, and a decrease of c and c/a.^[23] Both effects are counteracting in the NMC 801010 sample. The lattice parameter a is not significantly affected by Mg substitution content ≤2 mol%. These results are consistent with previous observations by Pouillerie et al. for Mg substitution amounts of ≤10 mol% in LiNiO₂. [19b] However, increasing the Mg content while decreasing the Mn content in NMC 900505 results in a small contraction in the c lattice parameter and c/a ratio. There seems to be a monotonic decrease in the Li⁺/Ni²⁺ cation mixing with increasing Mg content, being more noticeable when assuming Mg²⁺ only sits on the Li⁺ sites (Figure S4b, Supporting Information). Since the presence of Ni and/or Mg in the interslab can hardly be distinguished via X-ray and Rietveld refinement, the trend in the Li⁺/Ni²⁺ mixing seems to be strongly influenced by the hypothesis assumed to perform the refinements. The electron density in the interslab will be exceeded when considering the undifferentiated presence of both Ni and Mg ions in the 3a sites, [19a] thereby distorting the results. Nevertheless, a downward trend in cation mixing is noticeable with increasing Mg content/decreasing Mn content, while a slight increase in cation mixing was found when decreasing the overall Co content by 1 mol% (from 4.1 ± 0.1 (NMC 900505) to $4.6 \pm 0.1\%$ (NMC 90050401)). These results might be in agreement with previous works on Mg²⁺, $\mathrm{Co^{3+}}$, and $\mathrm{Mn^{4+}}$ substitution in $\mathrm{LiNiO_2}$. [13] While Co-substituted LiNiO₂ showed the lowest Li⁺/Ni²⁺ mixing for a certain substituent content, Mg-substituted LiNiO2 showed higher—but still relatively low-degree of cation mixing.

2.2. Electrochemical Characterization

Electrochemical characterization was first conducted in NMC || Li metal cells at various charge/discharge rates from 0.1 to 3C to evaluate the rate capability and stability at increasing upper operating cell voltages (4.3, 4.4 V vs 4.5 V). Results can be found in the supporting information (Figure S5, Supporting Information). For evaluating the rate capability up to a 3C discharge rate, asymmetric tests were performed at a constant 0.2C charge rate to minimize detrimental effects to the Li metal electrode. During formation cycles at 0.1C, discharge capacities in the range between \approx 207 ± 1 mAh g⁻¹ (NMC 900505) and $187.2 \pm 0.4 \text{ mAh g}^{-1}$ (NMCMg 90030502) are reached. Although variable experimental conditions make comparisons rather difficult, these values are in the same range of those reported in previous works on Ni-rich NMC materials for similar targeted stoichiometries with ≈90 mol% Ni. For instance, Li et al. reported a specific discharge capacity of 226 mAh g⁻¹ during 0.1C formation at a voltage operation window between 2.8 and 4.4 V for $LiNi_{0.890}Mn_{0.055}Co_{0.055}O_{2}$. The increase of Mg in the bulk of the material gradually decreases the delivered capacity

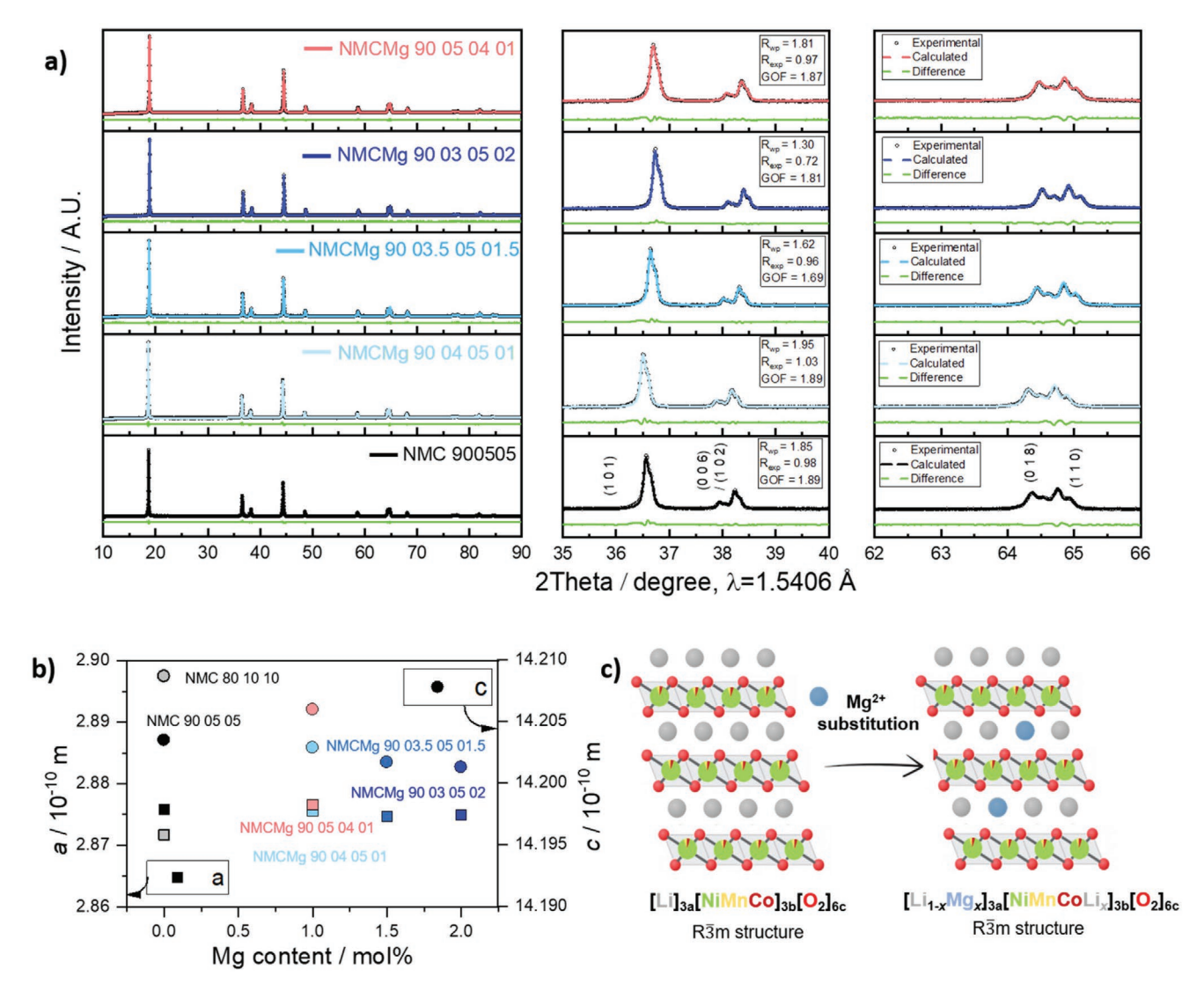


Figure 2. a) XRD patterns and representative Rietveld refinements of Ni-rich Mg-substituted cathode materials; b) Lattice parameters a and c determined by Rietveld refinement. Further details of the refinements can be found in the SI. Colored squares represent the lattice parameter a, while the lattice parameter c is represented as colored circles; c) Schematic illustration of the layered crystal structure of a Mg-substituted $[Li_{1-x}Mg_x]_{3a}[NiMnCoLi_x]_{3b}[O_2]_{6c}$ structure with R^3m space group symmetry.

due to Mg being electrochemically inactive (further details are discussed below). Specific discharge capacities are decreased to $\approx 172.1 \pm 0.3$ mAh g⁻¹ (NMC 900505) and $\approx 158 \pm 1$ mAh g⁻¹ (NMCMg 90030502) when increasing the discharge rate to 3C. Notably, the attainable capacities up to 3C normalized with respect to the capacities at 0.1C for each sample are similar to that of the reference NMC 900505 sample regardless of the Mg substituent content. Although the introduction of Mg ions reduces the initial capacity, the rate capability is thereby not adversely affected. Following the C-rate test, high voltage operation up to 4.4 and 4.5 V reveals an improved cycle life for Mgcontaining samples, outperforming the reference NMC 900505 cathode during cycling at 4.4 V (≈cycle 45th, Figure S5, Supporting Information). Cells containing Mg-substituted Ni-rich materials exhibit superior discharge capacities when charged to 4.5 V, probably due to lower capacity fading upon the prior C-rate investigations. Overall, these results imply that a proper content of Mg might play a key role in prolonging the cycling stability of Ni-rich cathode materials.

The practical application of Ni-rich cathode materials under realistic testing conditions was evaluated in NMC \parallel graphite full-cells within the cell voltage range 2.8–4.2 V in two-electrode configuration. **Figure 3**a,b shows the 1st cycle charge/discharge cell voltage profiles and differential capacity (dQ/dV) versus voltage plots of all the different Ni-rich Mg-substituted cathode materials in NMC \parallel graphite full-cells at 0.1C, respectively. As can be seen, the incorporation of Mg²⁺ into the NMC bulk causes evident changes in the voltage curve. Generally, four peaks can be observed in the dQ/dV versus voltage plots as lithium is extracted/inserted from/to the cathode material and can be attributed to the (de-)intercalation into graphite and phase transitions of the Ni-rich NMC cathode materials: kinetic hindrance region in H_1 phase, H_1 –M (\approx 3.65 V), M– H_2 (\approx 3.9 V), and H_2 – H_3 phase transition peaks (\approx 4.1 V). H and M

ENERGY

www.advancedsciencenews.com www.advenergymat.de

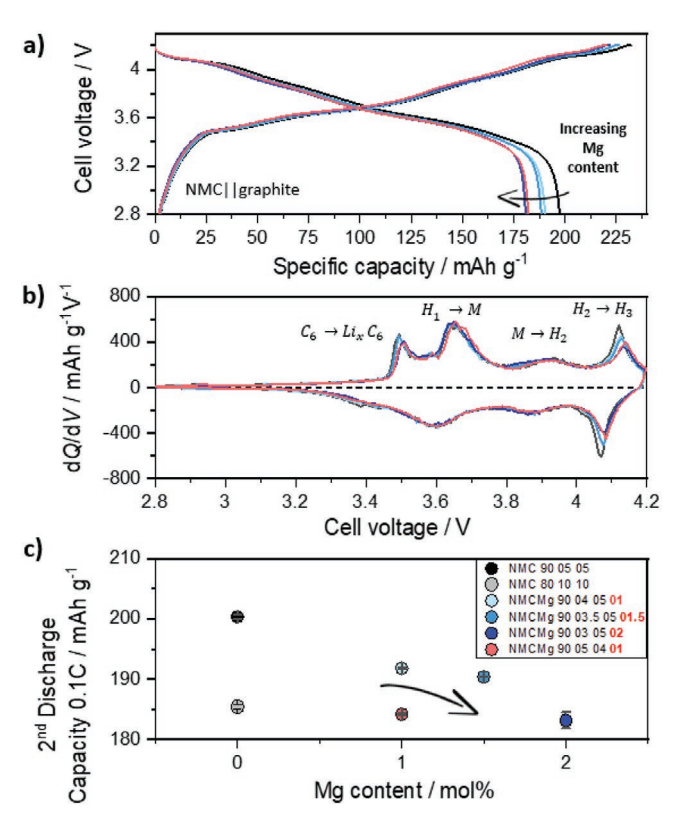


Figure 3. 1st cycle a) cell voltage profiles and b) corresponding differential capacity plots (dQ/dV) versus voltage plots of NMC || graphite cells at 20 °C within a cell voltage range of 2.8–4.2 V at 0.1C; c) 2nd discharge capacity as a function of Mg content for different Ni-rich NMC-type cathode materials. Error bars represent the standard deviation of three cells tested for each sample. N/P-ratio: 1.15:1.00, electrolyte: 1 M LiPF₆ in 3:7 vol% EC/EMC + 2 wt% VC. H and M refer to hexagonal and monoclinic phases and the different phase transitions are labeled as H₁–M, the M–H₂, and H₂–H₃ in the corresponding transition peaks. [4b]

refer to hexagonal and monoclinic phases, respectively.^[24] In the voltage range below 3.6 V, the reduction of electrolyte at the graphite anode and the formation of the solid electrolyte interphase (SEI^[25]) occur, followed by the lithium intercalation into graphite ($C_6 \rightarrow \text{Li}_x C_6$) at $\approx 3.45 \text{ V}.^{[26]}$ Although the characteristic plateaus along with sharp peaks in the dQ/dV versus voltage plot related to lithium/vacancy ordering processes upon (de-) lithiation are clearly visible for all cells, the inclusion of Mg within the 3a sites disturbs the lithium ordering and causes less pronounced anodic peaks in the corresponding dQ/dV versus voltage plots (from 3.8 to 4.2 V), giving evidence of suppressed phase transitions. [27] These observations have been reported for similar materials and are particularly evident in the H₂-H₃ phase transition region peak at high voltages, which is believed to be the responsible of an abrupt unit cell volume contraction and structure collapse due to the lattice mismatch between H₂ and H₃ phases. [4b,18a] Furthermore, the de-lithiation voltage is shifted to slightly higher values due to the lower lithium extraction ratio at the same operating voltage window.[18a] In order to avoid any influence of the graphite potential profile and reactions of the electrolyte with the graphite surface (e.g., SEI formation and growth) on evaluating the influence of Mg on the voltage profiles, Figure S6, Supporting Information, shows the 1st cycle charge/discharge cell voltage profiles and dQ/dV versus voltage plots of all Ni-rich Mg-substituted cathode materials in NMC \parallel Li-metal cells at 0.1C. As can be seen, three peaks originate from the transition of hexagonal to monoclinic to hexagonal phases ($H_1 \rightarrow M, M-H_2, H_2-H_3$) and confirm similar observations to those already made in NMC \parallel graphite full-cells, that is, the inclusion of Mg smoothes phase transitions.

With the incorporation of Mg²⁺ into the bulk, the initial delivered charge/discharge specific capacities follow a linear declining trend as the Mg substituent content is increased, in agreement with the NMC || Li metal cell results and previous works on Mg-substitution. [13,28] The 2nd cycle discharge capacity decreases from \approx 200.3 \pm 0.4 (NMC 900505) to 183 \pm 1 mAh g⁻¹ (NMCMg 90030502) when increasing the Mg content from 0 to 2 mol% at a fixed Ni content of 90 mol%, as shown in Figure 3c. Mg²⁺ being electrochemically inactive reduces the amount of delivered capacity by rendering inactive two Li atoms per Mg atom due to the formation of Ni⁴⁺ for charge balance. [13] This is a clear disadvantage compared to Al³⁺ substitution, which decreases the capacity only by one Li per Al, but the inclusion of Al during the co-precipitation causes disrupting particle growth due to the comparatively high tendency of Al3+ ions to precipitate in aqueous media, even at lower pH values. [5b,29] The capacity penalty with increasing substituent content is more noticeable for samples with less Co (NMCMg 90050401) despite only containing 1 mol% Mg, as the Co3+/Co4+ redox couple is active and also further contributes to the overall capacity.[3a] One should note that the 2nd cycle specific discharge capacity of samples with a higher degree of substitution (= 2 mol%) is similar to that of the NMC 801010 cathode. Similarly, the 1st cycle Coulombic efficiency (C_{Eff}, Figure S7a, Supporting Information) is also reduced with increasing Mg content from ≈85 (NMC 900505) to 83% (NMCMg 90030502), following the same trend and being slightly lower to those 1st cycle C_{Eff} reported in NMC || Li metal cells (Figure S7b, Supporting Information).[30] The 1st cycle irreversible capacity could be related to irreversible structural changes at both anode and cathode, and limitations in kinetics during the lithiation process.[31]

The long-term stability of Ni-rich layered oxides has been evaluated in practical NMC | graphite full-cell conditions to find the sweet spot between cycle life, reversible specific capacities and specific energies. Systematic electrochemical investigations of Mg-substituted Ni-rich NMC cathode materials in full-cells using different dopant concentrations have rarely been reported. Although a fair comparison of the electrochemical properties of different Mg-doped Ni-rich cathode from different studies is rather challenging due to differences in material preparation, and the lack of standardized testing protocols and electrochemical conditions, Table S3, Supporting Information, gives a comparison of electrochemical properties of previously reported Mg-substituted Ni-rich layered oxides. To the best of our knowledge, just the work of Xie et al. reported a significantly improved cycle life for Li_{0.98}Mg_{0.02}Ni_{0.94}Co_{0.06}O₂ materials with only a Mg content of 2 mol% in graphite-based full-cells, reaching 80.1% state-of-health (SOH) after 500 cycles. [6b] Ga $[r(Ga^{3+}) = 0.62 \text{ Å}]$ and $Zn[r(Zn^{2+}) = 0.74 \text{ Å}]$ are also substituents believed to occupy Li sites and playing a similar role to Mg²⁺ in enhancing cycle life, but only Zn has been introduced during

ADVANCED ENERGY MATERIALS

the co-precipitation. [32] After 500 cycles in graphite-based full-cells, Zn-doped $\text{LiNi}_{0.94}\text{Co}_{0.04}\text{Zn}_{0.02}\text{O}_2$ delivered a capacity retention of 74%.

After four formation cycles at 0.1C, long-term cycling was evaluated at 0.33C until reaching 80% SOH (based on the 5th cycle specific discharge capacity). A N/P ratio of 1.15:1.00 was used to avoid Li metal plating at the graphite negative electrode.[33] Figure 4a,b compare the long-term cycling performance of all synthetized cathode materials versus a graphite negative electrode. As can be seen, the initial specific capacity at 0.33C of cells containing Mg-substituted NMC materials is proportional to the substituent content. The same tendency is followed in cycle life, that is, cathode materials substituted with Mg show a superior cycle life and less pronounced capacity fading with respect to the reference NMC 900505 that despite the highest gravimetric capacity at the beginning, this capacity retained the least during cycling. While the NMC 900505 cells achieve 80% SOH after only ≈230 cycles, Mg-substituted cells cross the reference cells after only 100 cycles and reach 80% of the capacity after ≈350–600 cycles, depending on the Mg content. At first glance, these results suggest a remarkably improvement regarding cycle life by introducing Mg. These values outperform previous results by Xie et al. for a Li_{0.98}Mg_{0.02}Ni_{0.94}Co_{0.06}O₂ cathode material in graphitebased full-cells with only a Mg content of 2 mol%, reaching 80.1% SOH after 500 cycles. [6b] Notably, the cycling stability and specific capacities of NMC 90030502 are nearly on par with a NMC 801010 cathode synthetized through the same co-precipitation route.

Figure S8a, Supporting Information, shows the evolution of calculated specific energies during long-term cycling. Table S4, Supporting Information, gives an overview of electrochemical properties (specific capacities, mean discharge voltages, and calculated specific energies) of the different NMC materials. Considering their average discharge voltage and specific discharge capacities, initial specific energies (2nd cycle) on the material level (only based on the cathode active mass) of $\approx 746 \text{ Wh kg}^{-1}$ (NMC 900505), 714 Wh kg^{-1} (NMCMg 90040501), 710 Wh kg^{-1} (NMCMg 9003.50501.5), 684 Whkg⁻¹ (NMCMg 90030502), 687 Whkg⁻¹ (NMCMg 90050401), and 688 Whkg⁻¹ (NMC 801010) are achieved at a rate of 0.1C. The combination of high specific gravimetric capacities and high average discharge voltages fulfills the requirements of a high-energy LIB cell. With ongoing cycling, NMC 801010 and NMCMg 90030502 cells retain their initial specific energies better.

Figure 4c–g shows dQ/dV versus voltage curves to track the evolution of phase transitions during cycling (5th, 50th, 100th, 150th, and 200th cycle) for all cells. Overall, cells cycled with Mg-substituted cathodes exhibit a more stable cell voltage profile with ongoing cycling, consistent with the enhanced cycling stability shown in Figure 4a. The reference NMC 900505 sample suffers from irreversible phase transitions and gradual decay in intensity of the H_2 – H_3 peak, shifting to higher cell voltages due to increasing voltage polarization. In contrast, the dQ/dV versus voltage curves of Mg-substituted NMC cathodes exhibit more subtle changes and the intensity decay is not as abrupt as that of the reference cells, with little polarization development during cycling. However, the initial intensity of the H₂-H₃ peak is much more pronounced for the NMC 900505 sample, while Mg-substituted cathodes exhibit smoothened phase transitions. The evolution of the average discharge voltage (V) and the difference of the average charge and the average discharge voltages (ΔV) over cycling can be better seen in Figure 4h,i. ΔV (calculated by $V_{\rm average, charge}$ – $V_{\rm average, discharge}$ can provide information about the impedance of a cell, that is, higher ΔV values implicitly entail a higher cell impedance. [34] As can be seen, the evolution of average discharge voltage reveals a linear voltage fade as well as a steady increase in ΔV upon cycling. Despite similar voltage hysteresis at the beginning of the test for all samples, the hysteresis is severely increased for the less-substituted samples due to high impedance build-up evidenced by the increased voltage polarization. The higher impedance can be a result of oxygen loss from the materials, formed micro-cracks between primary particles and irreversible structural change leading to the formation of rock salt NiO-phases at the exposed surface in contact with the electrolyte, that increases cell impedance and hinders Li⁺ migration. The NMCMg 90030502 sample shows the smallest impedance growth upon cycling and a more stable average discharge voltage.

For further comparison between the electrochemical performance of the different cathode materials and lithium ion fullcells, the Coulombic inefficiencies for each cycle were calculated and accumulated over cycling. Figure S8b, Supporting Information, shows the evolution of accumulated Coulombic inefficiencies (ACI) as a function of the cycle number for the long-term experiments. ACIs can reflect parasitic reaction within the LIB cell, including reductive electrolyte decomposition during interphase formation (SEI and cathode electrolyte interphase, CEI^[35]), TM dissolution, and loss of active lithium. [36] During the formation cycles, cells with the NMC 900505 cathode show the lowest ACIs of ≈16% compared to NMCMg 90030502 (≈18%). However, the trend is reversed with ongoing charge/ discharge cycling: Mg-substituted samples reflect smaller slopes, indicating suppressed parasitic side reactions, though differences between samples are relatively small.

2.3. Post-Mortem SEM and Ex Situ XRD

To investigate the structural stabilities of the Ni-rich cathode materials, cycled electrodes after reaching 80% SOH were retrieved from the cells in discharged states and analyzed via SEM. Figure 5 shows representative cross-sectional SEM images via focused ion beam (FIB) of pristine and cycled electrodes for a, d) NMC 900505, b, e) NMCMg 90040501, and c, f) NMCMg 90030502 samples, respectively. As can be seen, all secondary particles of pristine materials are quite dense with small internal porosity between primary particles. The extent of micro-cracks after cycling correlates well with the electrochemical results and capacity fading discussed above. After cycling, the reference NMC 900505 material for only ≈230 cycles, severe formation of inter-granular cracks can be observed (Figure 5d). Large micro-cracks propagate to the outer surface of secondary particles (see red arrows), creating paths for electrolyte penetration, thus exposing new surfaces for potential parasitic side reactions and eventually particle fracture, pulverization, or disconnection with ongoing cycling. [4c] The formation of micro-cracks could be the dominant factor causing the enhanced capacity fading and the growth of cell impedance and

www.advancedsciencenews.com www.advenergymat.de

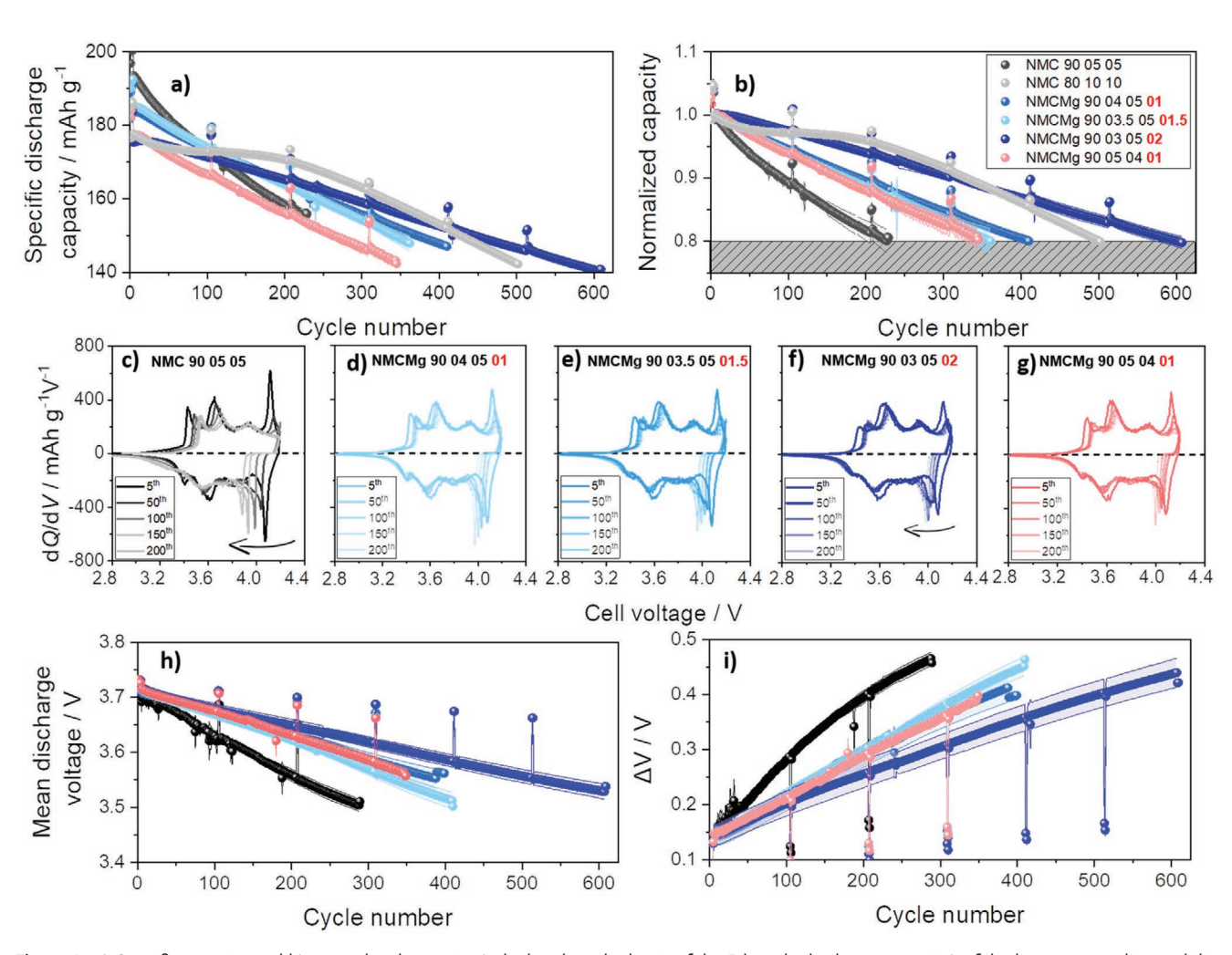


Figure 4. a) Specific capacity and b) normalized capacity (calculated on the basis of the 5th cycle discharge capacity) of the long-term cycling stability experiments on NMC || graphite full-cells at 0.33C ($1C = 190 \text{ mA g}^{-1}$); c–g) Evolution of differential capacity (dQ/dV) versus voltage plots, h) discharge-averaged mean voltage and i) difference between charge and discharge voltages (ΔV) of Ni-rich NMC cathodes versus graphite over cycling. Error bars represent the standard deviation of three cells tested for each sample. Cell voltage range: 2.8–4.2 V, N/P-ratio: 1.15:1.00, electrolyte: 1 M LiPF₆ in 3:7 vol% EC/EMC + 2 wt% VC.

voltage polarization shown above. In contrast, NMC 90040501 and NMC 90030502 samples (Figure 5e,f) retain their original microstructure and only contain narrow micro-cracks confined in the core of spherical particles, explaining their relatively good cycling performance with respect to the reference cells. Still, the highly reactive unprotected electrode surface at the electrode|electrolyte interface in highly de-lithiated states can lead to ongoing formation of a surface rock salt layer, contributing to the capacity fading as well. Future works should shed more light on the degradation mechanisms occurring at the surface of Ni-rich cathode materials and whether the presence of Mg can improve the stability of the surface during storage, for example, due to the stronger Mg—O covalent bond that might inhibit further chemical reaction between moisture/ carbon dioxide with the surface of Ni-rich layered oxides.

Interestingly, **Figure 6**a clearly shows a declining linear correlation between the attainable 2nd discharge capacity at 0.1C of all synthetized cathode materials against cycle life relative to the references NMC 900505 and NMC 801010.

As can be seen, the cycle life to 80% capacity was prolonged almost linearly with increasing the level of Mg substitution from 0 to 2 mol%, while the practical delivered capacity (and lithium extraction ratio considering the theoretical specific capacity of NMC as 278 mAh g-1[31]) was similarly decreased due to Mg being electrochemically inactive. These results are consistent with previous findings from Li et al. and Yoon et al. that pointed out that the cycle life in Li metal cells (oversimplifying called "half-cells"[37]) for polycrystalline cathode materials was mainly governed by the attainable specific capacity and the corresponding degree of de-lithiation and not by the Ni content.[4b,38] In our studies, there is no critical limit, where the stability is abruptly worsened, but rather there is a clear linear trend between maximum attainable capacity and cycle life. The only sample outside the trend is the sample with the least Co content (NMCMg 90050401), showing the highest degree of Li⁺/Ni²⁺ cation mixing at first but the poorest cycling stability despite the slightly lower initial capacity. Therefore, the decrease in Co

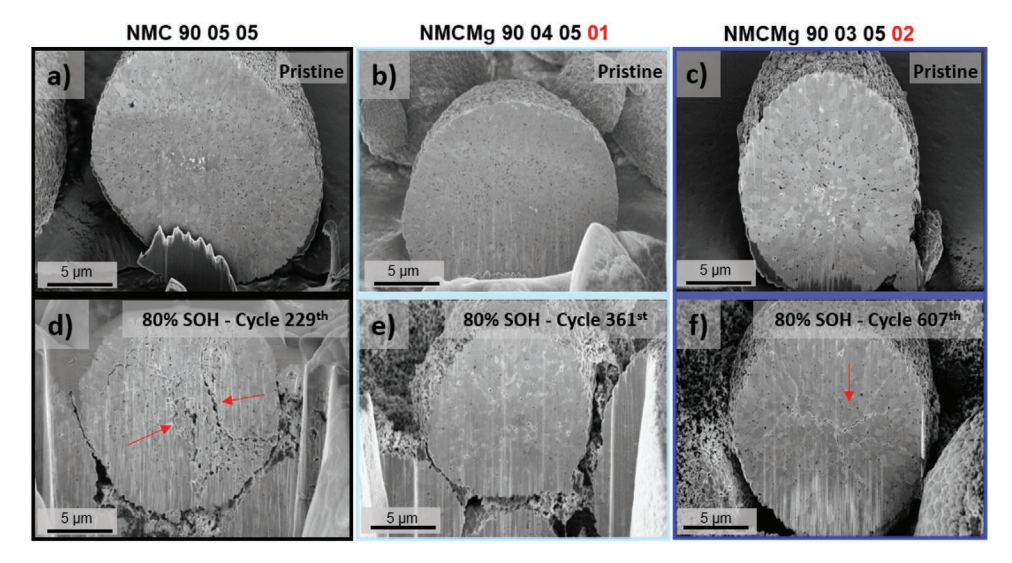


Figure 5. Cross-sectional SEM images of pristine and cycled a,d) NMC 900505; b,e) NMC 90040501; c,f) NMC 90030502 materials from NMC | graphite full-cells after reaching 80% SOH. The red arrows in (d) and (f) indicate the presence of micro-cracks.

below 5 mol% most likely has a significant detrimental effect on structural stability despite the substitution with Mg. However, looking at the accumulated specific energy upon cycling (Figure S9, Supporting Information) instead of considering the residual capacity at a certain cycle number reveals a significantly higher energy throughput through the reference NMC 900505 for the first 50 cycles in comparison to the Mg-substituted samples that might also explain the enhanced degradation. The superior performance remains until cycle 225th, at which point of operation time the NMCMg 90030502 cells outperforms the reference NMC 900505.

To shed light on the structural evolution and changes in lattice parameters and unit cell volume upon charging/discharging different materials to the same upper cut-off voltage of 4.2 V and alternatively to the same degree of de-lithiation (gravimetric specific capacity of 200 mAh g⁻¹, corresponding to a lithium extraction ratio of $x \approx 0.72$ in $\text{Li}_{1-x}TMO_2$), ex situ XRD measurements were performed on pristine and cycled cathode electrodes after the 2nd charge/discharge cycles at a rate of 0.1C. Figure 6b shows expanded views of the (003) Bragg reflection of representative Mg-substituted Ni-rich NMC cathodes (NMC 900505, NMCMg 90040501, and NMCMg 90030502). Detailed results of the Pawley analysis^[39] for all samples can be found in Figures S10-S14 and Table S5, Supporting Information. As can be seen, the NMC 900505 sample exhibits two (003) distinct reflections and a two-phase behavior (separation of the H₂ and H₃ phases) in the charge state up to 4.2 V (corresponding to a gravimetric capacity of ≈ 200 mAh g⁻¹) while the others samples exhibit a single reflection, confirming previous observations by dQ/dV versus voltage curves and suppressed phase transitions by substituting with Mg. The (003) reflection for all Mg-substituted cathode materials is shifted upon charging, but does not shift back to the original position after discharging, therefore lattice parameters and unit cell volume are not fully recovered due to irreversible reactions.

Figure 6c and Figure S10, Supporting Information, shows the changes normalized unit cell volume and lattice parameters

(a and c) in the pristine, charged and discharged states as a function of the Mg content, respectively. The lattice parameter a shows a decrease upon charging due to the oxidation of Ni ions. Such a decrease is more noticeable for the samples delivering higher capacities. In contrast, the lattice parameter c typically shows first an increase upon cycling which stems from a high electrostatic repulsion between the oxygen layers, but then shrinks abruptly at high degree of de-lithiation.[27,40] While the presence of the H₃ phase transition in NMC 900505 causes a collapse of the c-axis and a significant volume contraction of up to ≈5% due to the lattice mismatch between H₂ and H₃ phases, Mg-substituted cathode materials still show an increased c-lattice when charging to 4.2 V in comparison to the pristine electrodes. Therefore, samples containing Mg exhibit smoothed phase transitions and are not (de-)lithiated enough at the considered operating voltage window in NMC || Graphite full-cells (2.9–4.2 V); thereby, the materials suffer from a lower volume contraction when increasing substituent content. When charging all cells to the same upper cut-off voltage (4.2 V), one can thus assume that the H2-H3 phase transformation observed in the NMC 900505 sample has a detrimental effect on the long-term cycling performance due to the pronounced volume contraction and severe micro-crack formation. By increasing the Mg content, materials are less prone to develop micro-cracks, as result of the suppressed and lower anisotropic volume change due to the decreased delivered capacity and Li+ extraction ratio at a certain operating window voltage.

However, by charging all cathode materials (NMC 900505, NMCMg 90040501, and NMCMg 90030502) to the same lithium extraction ratio (x \approx 0.72 in Li_{1-x}TMO₂ considering the theoretical specific capacity of NMC as 278 mAh g⁻¹) and therefore same state-of-charge (SOC), volume change becomes more similar for the different samples. Interestingly, Mg-substituted samples even suffer from a larger contraction of the lattice parameter c and thus linearly increasing volume change when increasing the Mg content in comparison to the reference NMC 900505 sample. This could be attributed to the

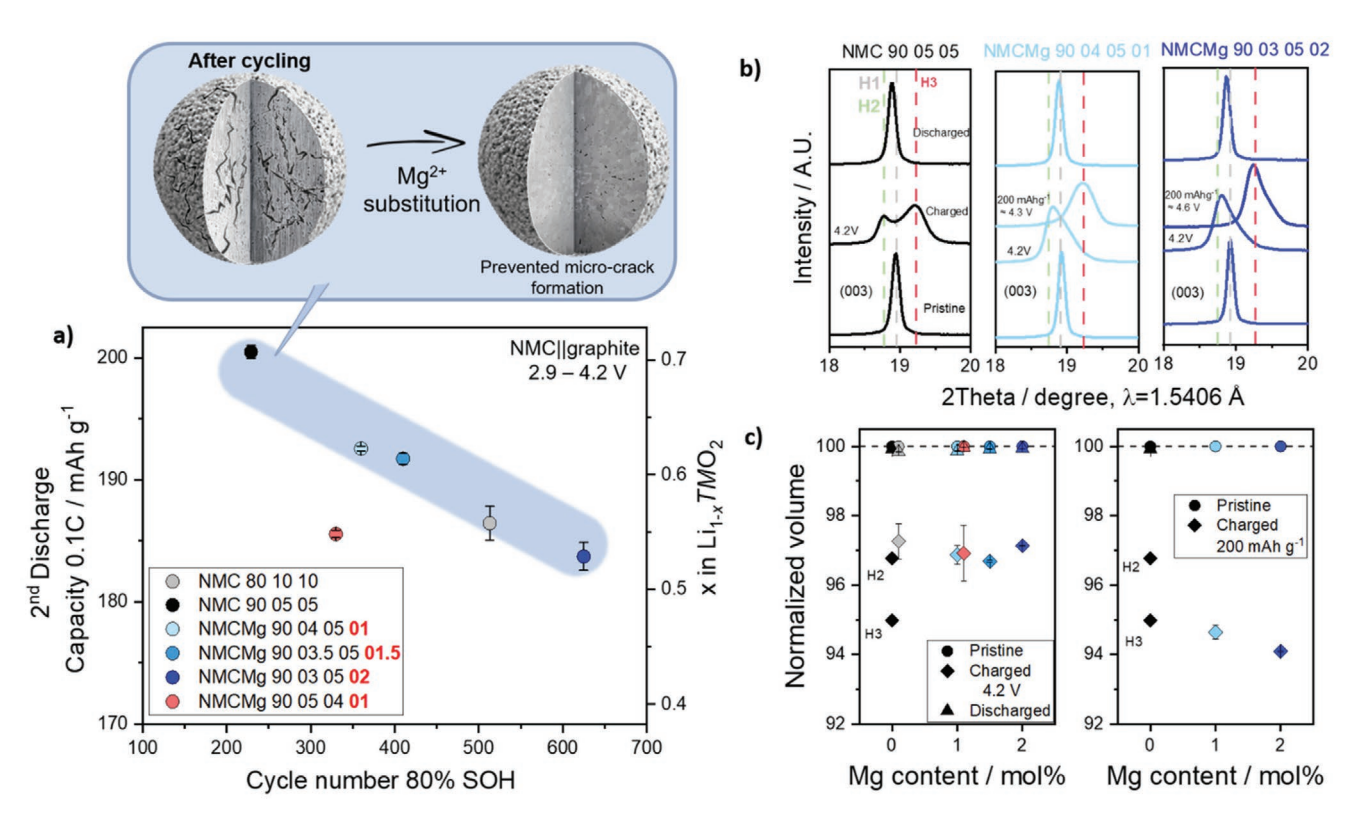


Figure 6. a) 2nd discharge specific capacity at a rate of 0.1C against the attainable cycle numbers to 80% SOH in NMC \parallel graphite full-cells. The SOH is based on the delivered capacity in the fifth cycle for all materials (1st cycle at 0.33C). Cell voltage range: 2.8–4.2 V, N/P-ratio: 1.15:1.00, electrolyte: 1 M LiPF₆ in 3:7 vol% EC/EMC + 2 wt% VC. b) Representative ex situ XRD patterns of Ni-rich Mg-substituted cathode electrodes in the pristine, charged (4.2 V and 200 mAh g⁻¹ ($x \approx 0.72$, in Li_{1-x} TMO_2 considering the theoretical specific capacity of NMC as 278 mAh g⁻¹) and discharged state (2.8 V; after charging to 4.2 V). Further details of the refinements can be found in the SI. H₂ and H₃ refer to hexagonal phase transitions upon (de-)lithiation of NMC materials. [4b]

different ionic radii of Li⁺ [$r(\text{Li}^+)$ = 0.76 Å] and Mg²⁺[$r(\text{Mg}^{2+})$ = 0.72 Å]. Assuming that Mg²⁺ sits in the Li sites and remains immobile upon lithiation/de-lithiation, the amount of the overall electrochemically active Li atoms in the Li interslab is reduced, and therefore for the "same" de-lithiation degree, the c-lattice should be smaller because of the smaller size of Mg²⁺. To reach the same SOC to that of the NMC 900505 sample in the voltage window 2.9–4.2 V, cells containing Mg-doped NMC cathode materials need to reach upper cell voltages of up to 4.6 V (Figure S10b, Supporting Information), which can cause degradation of carbonate-based electrolytes.

2.4. Thermal Stability of Mg-Substituted Ni-Rich NMC Materials in De-Lithiated State

Apart from cycle life and energy density, battery safety is always a major concern and important performance metric for the practical implementation of Ni-rich layered cathode materials. [28,41] The effect of Mg substitution on the thermal stability of charged Ni-rich cathodes was assessed via differential scanning calorimetry (DSC) analyses. For a head-to-head comparison, [5b] all cathode materials were charged to a specific capacity of 210 mAh g⁻¹, corresponding to the same SOC and degree of Li⁺ extraction ratio (\approx 75% based on the theoretical capacity of 278 mAh g⁻¹ for NMC).

Figure 7 shows the DSC analysis of de-lithiated samples in contact with fresh electrolyte. During thermal decomposition of NMC cathode materials there is a phase transition from the layered structure to disordered spinel structure (Fd3m) and finally to rock salt phase accompanied by subsequent O2 gas release at elevated temperatures (depending on the SOC and probably stoichiometry).[41,42] The reference sample NMC 900505 shows two exothermic peaks at 206 and 218 °C accompanied by a heat release of 1808 J g⁻¹. The exothermic peak temperatures are slightly shifted to 221 and 225 °C when increasing the Mg content on NMCMg 90040501 and NMCMg 90030502 samples, with released specific heat of 1790 and 2019 J g-1, respectively. These results indicate that introducing Mg²⁺ ions shift the onset of the exothermic reaction and phase transitions, but does not significantly impact the overall heat released. Similar decomposition temperatures (from 200 to 240 °C) and a shift to higher temperatures by substituting with Mg were also reported by Xie et al. [6b] and Li et al. [5b] using DSC analyses. Previous works have reported that an enhanced thermal stability by substituting with Mg2+ (considering that Mg2+ occupies Li+ sites) can be attributed to the inhibition/delay of Ni migration to octahedral sites in the highly de-lithiated degree and, hence, postpone the oxygen release and thermal failure. [6b,17,43] Moreover, the slight shift in thermal decomposition by partially substituting with Mg can stem from the

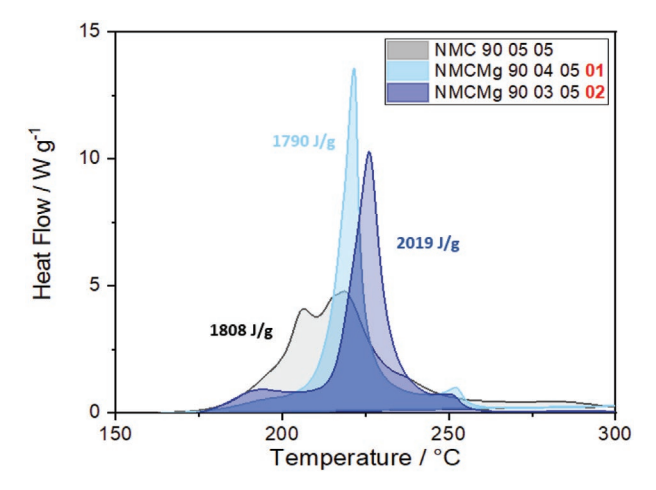


Figure 7. Representative DSC profiles of de-lithiated Ni-rich cathodes (NMC 900505, NMCMg 90040501, NMCMg 90030502) charged to 210 mAh $\rm g^{-1}$. Measurements were carried out in contact with the fresh electrolyte (1 M LiPF₆ in 3:7 vol% EC/EMC + 2 wt% VC).

higher standard enthalpies for formation of Mg-O (-601 kJ mol $^{-1}$) in comparison to that of Ni-O (-489.5 kJ mol $^{-1}$). $^{[15a]}$

2.5. Impact of Mg Substitution on Relevant Performance Metrics

High-nickel layered TM oxides (LiNi_xMn_yCo₂O₂, x > 0.80; x +y + z = 1) are regarded as the most promising cathode materials for next-generation LIBs for EV applications. In the ideal case, the cathode material should be an "all-rounder" possessing high specific energy/energy density on material level, excellent cyclic and thermal stability, and low raw material and production cost-all-in-one material. While the increase of the Ni content in NMC-type layered oxides to 90 mol% or more provides higher specific capacities (>190 mAh g⁻¹) and boosts the specific energy on material level, structural and thermal instabilities causing severe capacity fading strongly restrict their practical application. The incorporation of other cations within the bulk in small amounts, including Mg, is believed to enhance the electrochemical performance, in particular cycling stability. It is extensively reported in literature that Mg2+ ions are likely to sit on the lithium layer and act as pillars during the de-lithiation to improve the structural stability. [6b,19b] Although that might be true to some extent according to previous works performing in situ XRD experiments, [6b,17,19b] the question arises whether there is a beneficial impact of using Mg or the improved cycle life is related to the reduced capacity attained at a certain upper cut-off voltage and thus reduced volume contraction. Our results suggest such hypothesis and, as discussed in the previous section, the degree of de-lithiation could be equated for Mg-substituted samples by increasing the upper cut-off voltage limit to reach similar gravimetric capacities.^[44] However, results have also proven similar changes in unit cell volume, while high upper cut-off cell-voltages (4.3-4.6 V, depending on the Mg content), which are required to reach a similar SOC, can lead to several arising challenges, for example, oxidative decomposition of carbonate-based electrolytes, accelerated dissolution of TMs (TMs = Ni, Co, and Mn) in carbonate-based electrolytes

and the subsequent deposition at the graphite anode surface, leading to impedance increase due to the solid electrolyte interphase (SEI) degradation and significant cell capacity fade. [45] Therefore, the several degradation mechanisms concurrently taking place on both anode and cathode side might hinder the real influence of Mg in stabilizing the structure.

Figure 8 shows a qualitative comparison of cathode materials synthetized in this work via a radar diagram with respect to the foremost battery performance metrics for next generation LIBs. In summary, the inclusion of Mg substitution within Ni-rich NMC cathodes with a fixed Ni content of 90% sacrifices specific capacity and specific energy on material level when working at a certain voltage window. Nevertheless, the incorporation of Mg delays the thermal runaway and significantly enhances cycle life in comparison to the reference NMC 900505 cells, resulting in safer and structurally more stable materials. According to our results, the benefits of cationic substitution with Mg to the cycle life arise from the reduced capacity and thus a lower degree of anisotropic volume change upon (de-)lithiation. The best compromise between structural stabilization, cycle life, and gravimetric capacity falls in the range of 1-1.5 mol% Mg substitution. It is worth noting that the cycling stability in fullcells and specific capacities of NMCMg 90030502 are nearly on par with a NMC 801010 cathode, which is an already commercialized material. Similar electrochemical performance can thus be attained using 2 mol% Mg substitution, while allowing the decrease of the Co content by 5 mol% with respect to NMC 801010.

The linear trends between substituent concentration and specific capacities as well as cycle life reported herein might not be universal for all substitution species (= "dopants"), especially not for those dopants that promote a change in the shape of the primary particles, for example, from randomly oriented primary particles to elongated needle-like primary particles (e.g., W, B, Ta, etc.) and thus make the materials less prone to micro-crack formation.[10,46] We believe that more systematic investigations evaluating dopants on Ni-rich cathode materials to find the trade-off between cycle life and energy density are needed. However, apart from micro-crack formation, parasitic side reactions occurring at the electrodelelectrolyte interface in the highly de-lithiated state might need synergetic modification approaches. [47] To overcome the instability issues of Ni-rich cathode materials and allow the successful application of ultrahigh-Ni layered oxides, we believe that a variety of synthesis strategies should be pursued, including but not limited to bulk substitution, core/shell and gradient concentration designs, single-crystal morphology, and surface protections (coatings).

3. Conclusions

In this work, the impact of Mg substitution on structural and electrochemical properties of Ni-rich NMC-type layered oxides was comprehensively evaluated with respect to a reference NMC 900505 cathode material. Mg-substituted Ni-rich layered cathode materials with 90% Ni were synthetized by a co-precipitation method using a CTFR followed by calcination, resulting in cathode materials with excellent properties (narrow PSD, high tap density, low specific surface area, etc.) for practical

ENERG

www.advancedsciencenews.com

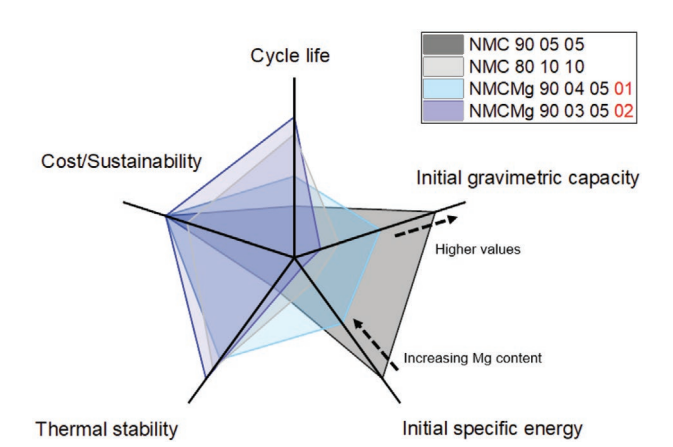


Figure 8. Comparison of synthetized layered cathode materials in terms of some key performance indicators.

application in high-energy LIB cells. The incorporation of Mg did not significantly affect particle morphology, PSD, surface area, and tap density of the materials, allowing a fair comparison of the individual impact of Mg on electrochemical properties.

The long-term cycle life of Ni-rich cathodes was evaluated in NMC | graphite full-cells under realistic testing conditions. Overall, increasing the Mg content from 1 to 2 mol% linearly reduced the initial capacities and specific energies due to Mg being electrochemically inactive, but the cycle life and thermal stability were significantly improved. As a rule, the cycle life within a given voltage window operation showed the following descending order for the investigated substituent content: 2 mol% Mg > 1.5 mol% Mg > 1.0 mol% > 0 mol% Mg. The extent of micro-crack formation within secondary particles until reaching 80% SOH and unit cell volume change upon charging correlated well with the capacity fading and extension of phase transitions upon (de-)lithiation.

The Mg substituent (dopant) content on Ni-rich NMC cathode requires precise optimization to significantly take a step toward practical implementation in high-energy LIB cells. With the use of 2% Mg, key performance metrics (specific energy, cycle life) are on par with those of the already commercially used NMC 801010 material with the added advantage of decreased content of Co as critical raw material. The addition of 1-1.5 mol% Mg improved the structural stabilization and cycle life without a significant penalty on capacity and specific energy at material level. Nonetheless, the pronounced capacity decay of all Ni-rich cathode materials remains a challenge not completely overcome by cationic substitution with Mg. Although this work can be of high value for researchers working on the development of Ni-rich cathode materials, we believe that a combination of different modification approaches such as core-shell design and surface coatings might be needed for the successful integration of NMC cathodes with Ni≥90% in practical LIB cells.

4. Experimental Section

Material Synthesis: All spherical Ni-rich hydroxide precursors were synthesized by a continuous co-precipitation process using a

1 L CFTR (Tera 3300, Laminar Co., Ltd.), as previously reported. [20] $Ni_{0.90}Mn_{0.05-x}Co_{0.05}Mg_x(OH)_2$ (x = 0, 0.01, 0.015, and 0.02) and $Ni_{0.90}Mn_{0.05}Co_{0.05-x}Mg_x(OH)_2$ (x = 0.01) precursors were synthesized by a conventional hydroxide co-precipitation method, and are referred to as "NMCMg" materials followed by the exact targeted stoichiometry. The effect of increasing the Mg content on LiNi_{0.90}Co_{0.05}Mn_{0.05}O₂ (denoted as the reference "NMC 900505" material), while decreasing Mn or Co content was evaluated in comparison to state-of-the-art $LiNi_{0.80}Co_{0.10}Mn_{0.10}O_2$ ("NMC 801010") synthetized using the same

co-precipitation process and without any further surface modification. The content of electrochemically inactive Mn⁴⁺ was decreased, with the

aim to not to largely sacrifice specific capacity when incorporating Mg²⁺. For the co-precipitation, a 1.5 M homogeneously mixed aqueous solution with the corresponding molar ratio of the reactant sulfate salts NiSO₄.6H₂O (98%, Alfa Aesar), CoSO₄.7H₂O (99%, Acros Organics), MnSO₄.H₂O (99%, Across Organics), and MgSO₄.7H₂O (98%, Sigma Aldrich) was fed into the reactor initially filled with distilled water. Simultaneously, a 4.875 M aqueous solution of NaOH (99.5%, Acros Organics) and a 12 wt% NH₃.H₂O solution as chelating agent (25%, Across Organics; molar ratio of ammonium hydroxide to TM = 1.2) were fed into the reactor at a controlled rate to maintain an ammonium hydroxide to TM ratio of 2.0. The co-precipitation reactions took place at a fixed temperature of 65 °C. The rotational speed of the inner cylinder of the reactor was set to 500 rpm to optimize the PSD and obtain relatively large secondary particles (≈10 µm). [20] The residence time of the CTFR was adjusted by the volume rates of the educts at 3 h. Reactants were fed into the reactor via membrane pumps (SIMDOS02, KNF). After 12 h to reach the steady state, the obtained precursors were collected, washed several times with deionized water, filtered, and dried at 80 °C overnight.

The precipitated hydroxide precursors were then homogeneously mixed with LiOH.H2O (98%, Fisher Chemical) by mortar and pestle in a lithium/TM molar ratio of 1.02 (Li:(Ni:Co:Mn:Mg) of 1:02:1) for a total mass of ≈6.5-7.5 g. An excess of lithium was used in order to compensate for lithium losses during the calcination process and thereby limit any lithium deficiency in the as-synthesized materials. Samples were first pre-calcined in a tube furnace (RS80/750/13, Nabertherm GmbH) for 3 h at 480 °C and then for 12 h at 750 °C under oxygen atmosphere. All heating steps used a heating rate of 2 °C min⁻¹ and an oxygen flow of 10 L h⁻¹. NMC 801010 was calcined up to 800 °C for comparison purposes. [48] Lithiated samples were ground with a mortar and pestle once more before further analysis to prevent agglomeration of secondary particles.

Material Characterization: Powder XRD (Bruker D8 Advance) of powdered samples was carried out using a Bragg-Brentano geometry between 10° and 90° at a step size of 0.02° s⁻¹ using Cu-K $_{\alpha}$ radiation (λ = 0.154 nm) at 30 kV and 10 mA. A 0.5 mm divergence slit was used for the measurements. Collected data were Rietveld refined using the Topas Academic V6 (Bruker AXS GmbH) based on a hexagonal α-NaFeO2 structure with a space group R-3m using the fundamental parameters approach.[49] For the refinements, Li was assumed to occupy 3a sites, TMs such as Ni, Co, and Mn were assumed to occupy 3b sites and oxygen was assumed to occupy 6c sites. The occupation of Ni^{2+} in the lithium layer was also quantified to account for the Li^+/Ni^{2+} mixing disorder due to the similar ionic radii ($r_{Ni}^{2+} = 0.69$ Å; $r_{\rm Li}^+=0.76$ Å). Although it was previously reported that Mg²⁺ ions are likely to only occupy Li⁺ sites (for concentrations <10 mol%),^[19a] six different hypotheses and refinement models were carefully evaluated for the placement of Mg²⁺ in the NMC structure and the determination of lattice parameters: i) refinements without considering Mg; ii) Mg only occupying 3b sites (TMs layer); iii) Mg occupying both 3a (Li layer) and 3b sites (TMs layer); iv) Mg occupying 3a sites (Li layer) and Li on 3b sites (TMs layer); v) Mg occupying 3a sites (Li layer) with vacancies on 3b sites and vi) Mg occupying 3a sites (Li layer) and TM layer with no vacancies. Constrains were added to maintain the overall stoichiometry. Crystallographic lattice parameters were considered based on the best goodness of fit. Detailed results can be found in the Supporting Information.



The particle morphology and elemental distribution of pristine materials were investigated by SEM and EDX using a Carl Zeiss AURIGA field emission microscope with a Schottky field emitter as electron source. The typical accelerating voltage was 3 kV. EDX was determined via a X-Max 80 mm² detector (Oxford Instruments) at 20 kV operating voltage. FIB-SEM milling was carried out to pristine powders at a milling current of 2 nA and 30 kV as acceleration voltage to quantify internal porosity and distribution of primary particles.

The chemical composition of the Ni-rich cathode materials was determined using ICP-OES (Spectro ARCOS EOP) with an axial positioned plasma torch. Measurements conditions were applied according to Vortmann and Evertz et al. $^{[50]}$

The tap densities of the precursors and lithiated cathode materials were determined by an Autotap tapped density analyzer (Quantachrome Instruments). For that, 2 g of material within a measuring cylinder was tapped for 10 000 times to determine the tapped volume. Measurements were repeated twice. The PSD of precursor and lithiated product was analyzed by laser diffraction (CILAS 1064) using aqueous conditions and dish soap as dispersant. Measurements were repeated three times to ensure a high reproducibility.

The specific or Brunauer–Emmet–Teller surface area of lithiated cathode powders was investigated by nitrogen adsorption at –196 °C on a 3Flex 3500 device (Micromeritics GmbH). Before the measurements, the powdered samples were degassed at 200 °C overnight under reduced pressure with a VacPrep 061 (Micromeritics GmbH).

Electrode Preparation: The Ni-rich positive electrodes consisted of 94 wt% active material, 3 wt% carbon black as conductive agent (Super C65, Imerys Graphite & Carbon) and 3 wt% poly(vinylidene difluoride) (PVdF) as binder (Solef 5130, Solvay). N-methyl-2-pyrrolidone (NMP, anhydrous, purity: 99.5%, Sigma-Aldrich) was used as solvent, reaching a solid content of 50 wt%. For paste preparation, the PVdF binder was first dissolved in NMP, followed by the addition of Super C65 and active material. The electrode paste was then homogenized by a high-energy disperser (Dissolver Dispermat LC30, VMAGetzmann GmbH) at a speed of 10000 rpm for 1 h. After complete dispersion, the paste was coated on Al foil (20 µm, Nippon foil) previously washed with ethanol using a doctor-blade (Zehntner GmbH) and an automatic film applicator (Sheen Instruments). Afterward, the electrode sheets were dried for 2 h in an atmospheric oven at 80 °C, punched out in 14 mm diameter discs, and then dried in a Büchi B-585 glass drying oven under reduced pressure ($<5 \times 10^{-2}$ bar) at 120 °C for 12 h. The average active material mass loading was \approx 5.0 \pm 0.2 mg cm⁻² for NMC || Li metal cell investigations and 12.0 \pm 0.5 mg cm $^{-2}$ for NMC \parallel graphite full-cell investigations, resulting in areal capacities of $\approx 0.98 \pm 0.3$ and $\approx 2.30 \pm 0.06$ mAh cm⁻², respectively, based on the 2nd cycle discharge capacity from NMC || Li metal cells. Electrodes were densified to reach a porosity of 35% using a hydraulic hand-press (Graseby Specac press, 2 tons cm⁻² for 15 s).

The negative electrodes used for full-cell investigations consisted of 95 wt% commercial synthetic graphite as the active material, 1.5 wt% styrene-butadiene-rubber (SB5521, LIPATON; Polymer Latex GmbH) and 3.0 wt% sodium-carboxymethyl cellulose (Na-CMC, Walocel CRT 2000 PPA12, Dow Wolff Cellulosics) as binders, and 0.5 wt% carbon black as conductive agent (Super C65, Imerys Graphite & Carbon). De-ionized water was used as solvent for paste preparation. The paste viscosity was optimized to reach a solid content of 40 wt% and homogenized as described above. The negative electrode paste was cast onto smooth copper foil (10 μ m, Nippon foil). After drying and calendaring the graphite sheets to achieve 30% porosity, $\emptyset = 15$ mm circular electrodes were punched out, and the electrodes were dried in a Büchi B-585 glass drying oven under reduced pressure (<5×10 $^{\!-2}$ bar) at 120 $^{\circ}\text{C}$ for 12 h. The average active mass loading of the negative electrodes was \approx 7.4 \pm 0.2 mg cm⁻², resulting in an areal capacity of \approx 2.6 \pm 0.1 mAh cm⁻² based on the practical capacity of graphite (≈350 mAh g⁻¹) obtained from the 2nd cycle discharge capacity from graphite || Li metal cell investigations.

Cell Assembly and Electrochemical Characterization: Electrochemical investigations were carried out in two-electrode configuration in coin cells (CR2032, Hohsen Corporation). [37] All cells were assembled in

a dry room atmosphere with a dew point of at least $-50~^{\circ}C$ (relative humidity of 0.16%). LP57 (1 $\,$ LiPF $_6$ in 3:7 vol% ethylene carbonate/ethyl methyl carbonate, EC/EMC, Solvionic) with 2 wt% vinylene carbonate (VC, 99.9%) as SEI additive was used as the electrolyte. A polymer membrane (1-layer, 16 mm Ø, Celgard 2500, Celgard) soaked with 35 μL of electrolyte was used as separator. The C-rate capability and long-term stability of Ni-rich cathode materials were investigated in NMC \parallel Li metal and NMC \parallel graphite full-cells, respectively. Three cells per sample were assembled to ensure a high reproducibility of our results. The standard deviation between different cells is represented as error bars in the corresponding figures.

For NMC \parallel Li metal cells, Ni-rich layered oxides as positive electrode (Ø14 mm, areal capacity of $\approx\!0.98\pm0.3$ mAh cm $^{-2}$) and a Li metal negative electrode (Ø15 mm, lithium metal foil, 500 μm in thickness; battery grade: purity $\geq\!99.9\%$, China Energy Lithium (CEL Co.)) were used. For NMC \parallel graphite full-cell investigations, Ni-rich layered oxides as positive electrode (Ø14 mm, areal capacity of $\approx\!2.30\pm0.06$ mAh cm $^{-2}$) and a graphite negative electrode (Ø15 mm, areal capacity of $\approx\!2.65\pm0.07$ mAh cm $^{-2}$) were considered. The negative/positive (N/P) capacity balancing ratio was set to 1.15:1.00 based on the 2nd discharge capacities from Li metal cell investigations. $^{[33]}$

Electrochemical properties were investigated via constant current (CC) charge–discharge cycling on a Maccor Series 4000 battery tester (Maccor, Inc.) at 20 °C. The specific current for a rate of 1C was defined as 190 mA g⁻¹. The rate capability of cathode materials at different upper cut-off voltages was first investigated in two-electrode configuration NMC || Li metal cells according to the following procedure: 6 h at opencircuit-voltage followed by two formation cycles at 0.1C, 3 cycles at 0.2C, and 5 cycles at 0.33, 0.5, 1, and 3C each. Asymmetric tests were performed at a constant 0.2C charge rate, while the discharge rate ranged between 0.1 and 3C. The cell voltage window up to this point was between 2.9 and 4.3 V. After the C-rate test, cells were cycled back at 0.1C for two cycles, followed by 15 cycles at 0.33C at different upper cut-off voltages: 4.3, 4.4, and 4.5 V.

The long-term cycle life of cathode materials was evaluated in NMC || graphite full-cells within the cell voltage range of 2.8–4.2 V. For that, cells were cycled for four cycles at 0.1C for interphase formation, followed by cycling at 0.33C until dropping to 80% SOH. Each 100 cycles, cells were cycled at 0.1C again for two cycles to evaluate capacity retention. After each charge step, a constant voltage step was performed with the limiting conditions of either achieving a time limit of maximum 30 min or when the specific current reaches values below 0.05C.

Post-Mortem Characterization: The surface morphology and intergranular crack evolution in secondary particles on the cycled Ni-rich layered cathodes (after reaching 80% SOH) was investigated by FIB-SEM as previously described. Prior to analysis, the cells were disassembled in the discharge state at 2.8 V in dry atmosphere (dry room) and the electrode surfaces were rinsed with 300 µL of dimethyl carbonate (DMC) to remove salt impurities. After a short drying period under reduced pressure, the electrodes were transferred into the SEM via a vacuumsealed sample holder to avoid exposure to atmospheric air. Pristine and cycled electrodes (after 2nd cycle charge/discharge) were analyzed by powder XRD as previously described to evaluate changes in lattice parameters (a and c) and unit cell volume. Cells were charged to the same upper cut-off voltage (4.2 V) or to the same SOC (gravimetric specific capacity of 200 mAh g⁻¹, corresponding to a lithium extraction ratio of $x \approx 0.72$ in Li_{1-x}TMO₂) without upper cut-off voltage limitation. Collected data was Pawley-refined using the Topas Academic V6 (Bruker AXS GmbH). [39]

Thermal Stability: The thermal stability of Ni-rich positive electrodes in their de-lithiated state was evaluated via DSC (Q2000, TA Instruments). The cathodes were charged for three formation cycles within the cell voltage range 2.8–4.2 V, and then cycled all materials up to 210 mAh g $^{-1}$ in NMC \parallel graphite full-cells for a fair comparison of the effect of different dopant concentrations. $^{[28]}$ The cells were then disassembled in the dry room and rinsed with 300 μL of DMC. The cathode was then dried and sealed tightly in a 100 μL high-pressure stainless-steel pan with a gold-plated copper seal with 7 μL of fresh electrolyte (1 M LiPF $_6$ in 3:7 vol% EC/EMC + 2 wt% VC, Solvionic). The



www.advenergymat.de

ADVANCED ENERGY MATERIALS

studies were conducted from 30 to 350 $^{\circ}\text{C}$ with a 5 $^{\circ}\text{C}$ min $^{-1}$ heating rate under argon atmosphere.

Supporting Information

Supporting Information is available from the Wiley Online Library or from the author.

Acknowledgements

The authors thank the European Union for funding this work in the project "SeNSE": This project has received funding from the European Union's Horizon 2020 research and innovation program under grant agreement No 875548. The authors thank Debbie Berghus and Verena Naber for performing DSC and ICP measurements, respectively. The authors also thank Andre bar for his graphical support. The authors thank Laminar Co., Ltd. for constant technical support for the Couette—Taylor Flow Reactor. The authors thank Solvionic for supply of electrolyte. Open access funding enabled and organized by Projekt DEAL.

Conflict of Interest

The authors declare no conflict of interest.

Data Availability Statement

Research data are not shared.

Keywords

cathode materials, lithium ion batteries, low-cobalt cathodes, Mg substitution, nickel-rich layered oxides

Received: September 30, 2021 Revised: December 13, 2021 Published online: January 5, 2022

- [1] a) J. Betz, G. Bieker, P. Meister, T. Placke, M. Winter, R. Schmuch, Adv. Energy Mater. 2019, 9, 1803170; b) R. Schmuch, R. Wagner, G. Hörpel, T. Placke, M. Winter, Nat. Energy 2018, 3, 267; c) M. Winter, B. Barnett, K. Xu, Chem. Rev. 2018, 118, 11433.
- [2] a) W. Li, E. M. Erickson, A. Manthiram, *Nat. Energy* 2020, 5, 26;
 b) S.-T. Myung, F. Maglia, K.-J. Park, C. S. Yoon, P. Lamp, S.-J. Kim, Y.-K. Sun, *ACS Energy Lett.* 2017, 2, 196.
- [3] a) A. Manthiram, Nat. Commun. 2020, 11, 1550; b) A. Manthiram,
 B. Song, W. Li, Energy Storage Mater. 2017, 6, 125; c) D. Andre,
 S.-J. Kim, P. Lamp, S. F. Lux, F. Maglia, O. Paschos, B. Stiaszny,
 J. Mater. Chem. A 2015, 3, 6709.
- [4] a) T. Li, X.-Z. Yuan, L. Zhang, D. Song, K. Shi, C. Bock, Electrochem. Energy Rev. 2020, 3, 43; b) H. Li, A. Liu, N. Zhang, Y. Wang, S. Yin, H. Wu, J. R. Dahn, Chem. Mater. 2019, 31, 7574; c) G. W. Nam, N.-Y. Park, K.-J. Park, J. Yang, J. Liu, C. S. Yoon, Y.-K. Sun, ACS Energy Lett. 2019, 4, 2995; d) S. Lee, W. Li, A. Dolocan, H. Celio, H. Park, J. H. Warner, A. Manthiram, Adv. Energy Mater. 2021, 11, 2100858; e) K.-J. Park, J.-Y. Hwang, H.-H. Ryu, F. Maglia, S.-J. Kim, P. Lamp, C. S. Yoon, Y.-K. Sun, ACS Energy Lett. 2019, 4, 1394; f) S. Klein, P. Bärmann, T. Beuse, K. Borzutzki, J. E. Frerichs, J. Kasnatscheew, M. Winter, T. Placke, ChemSusChem 2021, 14, 595; g) M. Evertz, F. Horsthemke, J. Kasnatscheew, M. Börner, M. Winter, S. Nowak, J. Power Sources 2016, 329, 364.

- [5] a) U.-H. Kim, L.-Y. Kuo, P. Kaghazchi, C. S. Yoon, Y.-K. Sun, ACS Energy Lett. 2019, 4, 576; b) W. Li, S. Lee, A. Manthiram, Adv. Mater. 2020, 32, 2002718.
- [6] a) W. M. Seong, A. Manthiram, ACS Appl. Mater. Interfaces 2020, 12, 43653; b) Q. Xie, W. Li, A. Manthiram, Chem. Mater. 2019, 31, 938.
- [7] Z. Yang, L. Mu, D. Hou, M. M. Rahman, Z. Xu, J. Liu, D. Nordlund, C.-J. Sun, X. Xiao, F. Lin, Adv. Energy Mater. 2021, 11, 2002719.
- [8] a) U. H. Kim, D. W. Jun, K. J. Park, Q. Zhang, P. Kaghazchi, D. Aurbach, D. T. Major, G. Goobes, M. Dixit, N. Leifer, C. M. Wang, P. Yan, D. Ahn, K. H. Kim, C. S. Yoon, Y. K. Sun, Energy Environ. Sci. 2018, 11, 1271; b) H.-H. Ryu, G.-T. Park, C. S. Yoon, Y.-K. Sun, J. Mater. Chem. A 2019, 7, 18580.
- [9] F. Schipper, H. Bouzaglo, M. Dixit, E. M. Erickson, T. Weigel, M. Talianker, J. Grinblat, L. Burstein, M. Schmidt, J. Lampert, C. Erk, B. Markovsky, D. T. Major, D. Aurbach, Adv. Energy Mater. 2018, 8, 1701682.
- [10] U.-H. Kim, G.-T. Park, B.-K. Son, G. W. Nam, J. Liu, L.-Y. Kuo, P. Kaghazchi, C. S. Yoon, Y.-K. Sun, Nat. Energy 2020, 5, 860.
- [11] a) D. Kong, J. Hu, Z. Chen, K. Song, C. Li, M. Weng, M. Li, R. Wang, T. Liu, J. Liu, M. Zhang, Y. Xiao, F. Pan, Adv. Energy Mater. 2019, 9, 1901756; b) T. R. Penki, S. Gilady, P. K. Nayak, H. Sclar, Y. Elias, J. Grinblat, M. Talianker, B. Markovsky, C. Erk, S. Luski, D. Aurbach, J. Solid State Electrochem. 2021, 25, 1513.
- [12] a) K. Zhou, Q. Xie, B. Li, A. Manthiram, Energy Storage Mater. 2021, 34, 229; b) L. Mu, R. Zhang, W. H. Kan, Y. Zhang, L. Li, C. Kuai, B. Zydlewski, M. M. Rahman, C.-J. Sun, S. Sainio, M. Avdeev, D. Nordlund, H. L. Xin, F. Lin, Chem. Mater. 2019, 31, 9769; c) C. S. Yoon, U.-H. Kim, G.-T. Park, S. J. Kim, K.-H. Kim, J. Kim, Y.-K. Sun, ACS Energy Lett. 2018, 3, 1634.
- [13] H. Li, M. Cormier, N. Zhang, J. Inglis, J. Li, J. R. Dahn, J. Electrochem. Soc. 2019, 166, A429.
- [14] A. Liu, N. Zhang, J. E. Stark, P. Arab, H. Li, J. R. Dahn, J. Electrochem. Soc. 2021, 168, 040531.
- [15] a) Y. Kim, W. M. Seong, A. Manthiram, Energy Storage Mater. 2021, 34, 250; b) H.-H. Ryu, H. H. Sun, S.-T. Myung, C. S. Yoon, Y.-K. Sun, Energy Environ. Sci. 2021, 14, 844.
- [16] A. Liu, J. Li, R. Shunmugasundaram, J. R. Dahn, J. Electrochem. Soc. 2017, 164, A1655.
- [17] X. Liu, S. Wang, L. Wang, K. Wang, X. Wu, P. Zhou, Z. Miao, J. Zhou, Y. Zhao, S. Zhuo, J. Power Sources 2019, 438, 227017.
- [18] a) A. Liu, N. Zhang, H. Li, J. Inglis, Y. Wang, S. Yin, H. Wu, J. R. Dahn, J. Electrochem. Soc. 2019, 166, A4025; b) B. Huang, X. Li, Z. Wang, H. Guo, X. Xiong, Ceram. Int. 2014, 40, 13223; c) H. Kondo, Y. Takeuchi, T. Sasaki, S. Kawauchi, Y. Itou, O. Hiruta, C. Okuda, M. Yonemura, T. Kamiyama, Y. Ukyo, J. Power Sources 2007, 174, 1131.
- [19] a) C. Pouillerie, L. Croguennec, P. Biensan, P. Willmann, C. Delmas, J. Electrochem. Soc. 2000, 147, 2061; b) C. Pouillerie, L. Croguennec, C. Delmas, Solid State Ionics 2000, 132, 15.
- [20] R. Schmuch, V. Siozios, M. Winter, T. Placke, Mater. Matters 2020, 15. 53.
- [21] a) M. Seenivasan, C.-C. Yang, S.-h. Wu, W.-C. Chien, Y.-S. Wu, R. Jose, S. J. Lue, J. Alloys Compd. 2021, 857, 157594; b) J. Helbig, T. Beuse, V. Siozios, T. Placke, M. Winter, R. Schmuch, Electrochim. Acta 2021, 366, 137413; c) J.-M. Kim, S.-M. Chang, J. H. Chang, W.-S. Kim, Colloids Surf. A 2011, 384, 31; d) J.-E. Kim, W.-S. Kim, Cryst. Growth Des. 2017, 17, 3677; e) N. Ohmura, K. Kataoka, Y. Shibata, T. Makino, Chem. Eng. Sci. 1997, 52, 1757; f) D. H. Jeon, J.-H. Song, J.-P. Hong, S. H. Lee, J. Ind. Eng. Chem. 2019, 76, 524.
- [22] L. Liu, M. Li, L. Chu, B. Jiang, R. Lin, X. Zhu, G. Cao, Prog. Mater. Sci. 2020, 111, 100655.
- [23] M. Bianchini, M. Roca-Ayats, P. Hartmann, T. Brezesinski, J. Janek, Angew. Chem., Int. Ed. 2019, 58, 10434.
- [24] H. Li, N. Zhang, J. Li, J. R. Dahn, J. Electrochem. Soc. 2018, 165, A2985.

www.advancedsciencenews.com www.adveners

www.advenergymat.de

ENERG

- [25] M. Winter, Z. Phys. Chem. 2009, 223, 1395.
- [26] J. Vidal Laveda, J. E. Low, F. Pagani, E. Stilp, S. Dilger, V. Baran, M. Heere, C. Battaglia, ACS Appl. Energy Mater. 2019, 2, 7036.
- [27] L. de Biasi, A. Schiele, M. Roca-Ayats, G. Garcia, T. Brezesinski, P. Hartmann, J. Janek, ChemSusChem 2019, 12, 2240.
- [28] M. M. E. Cormier, N. Zhang, A. Liu, H. Li, J. Inglis, J. R. Dahn, J. Electrochem. Soc. 2019, 166, A2826.
- [29] H. Z. Zhang, C. Liu, D. W. Song, L. Q. Zhang, L. J. Bie, J. Mater. Chem. A 2017, 5, 835.
- [30] J. Xiao, Q. Li, Y. Bi, M. Cai, B. Dunn, T. Glossmann, J. Liu, T. Osaka, R. Sugiura, B. Wu, J. Yang, J.-G. Zhang, M. S. Whittingham, *Nat. Energy* 2020, 5, 561.
- [31] J. Kasnatscheew, M. Evertz, B. Streipert, R. Wagner, R. Klöpsch, B. Vortmann, H. Hahn, S. Nowak, M. Amereller, A. C. Gentschev, P. Lamp, M. Winter, Phys. Chem. Chem. Phys. 2016, 18, 3956.
- [32] a) D. Kitsche, S. Schweidler, A. Mazilkin, H. Geßwein, F. Fauth, E. Suard, P. Hartmann, T. Brezesinski, J. Janek, M. Bianchini, Mater. Adv. 2020, 1, 639; b) Z. Cui, Q. Xie, A. Manthiram, ACS Appl. Mater. Interfaces 2021, 13, 15324.
- [33] J. Kasnatscheew, T. Placke, B. Streipert, S. Rothermel, R. Wagner, P. Meister, I. C. Laskovic, M. Winter, J. Electrochem. Soc. 2017, 164, A2479.
- [34] J. C. Burns, N. N. Sinha, G. Jain, H. Ye, C. M. VanElzen, W. M. Lamanna, A. Xiao, E. Scott, J. Choi, J. R. Dahn, J. Electrochem. Soc. 2012, 159, A1105.
- [35] D. R. Gallus, R. Wagner, S. Wiemers-Meyer, M. Winter, I. Cekic-Laskovic, Electrochim. Acta 2015, 184, 410.
- [36] F. Holtstiege, A. Wilken, M. Winter, T. Placke, Phys. Chem. Chem. Phys. 2017, 19, 25905.
- [37] R. Nölle, K. Beltrop, F. Holtstiege, J. Kasnatscheew, T. Placke, M. Winter, *Mater. Today* 2020, 32, 131.

- [38] C. S. Yoon, K.-J. Park, U.-H. Kim, K. H. Kang, H.-H. Ryu, Y.-K. Sun, Chem. Mater. 2017, 29, 10436.
- [39] V. Pecharesky, P. Zavalij, Fundamentals of Powder Diffraction and Structural Characterization of Materials, Springer US, New York 2005.
- [40] W. Li, H. Y. Asl, Q. Xie, A. Manthiram, J. Am. Chem. Soc. 2019, 141, 5097.
- [41] L. Geng, J. Liu, D. L. Wood, Y. Qin, W. Lu, C. J. Jafta, Y. Bai, I. Belharouak, ACS Appl. Energy Mater. 2020, 3, 7058.
- [42] S.-M. Bak, E. Hu, Y. Zhou, X. Yu, S. D. Senanayake, S.-J. Cho, K.-B. Kim, K. Y. Chung, X.-Q. Yang, K.-W. Nam, ACS Appl. Mater. Interfaces 2014, 6, 22594.
- [43] K. Min, S.-W. Seo, Y. Y. Song, H. S. Lee, E. Cho, Phys. Chem. Chem. Phys. 2017, 19, 1762.
- [44] Q. Xie, Z. Cui, A. Manthiram, Adv. Mater. 2021, 33, 2100804.
- [45] a) I. Cekic-Laskovic, N. von Aspern, L. Imholt, S. Kaymaksiz,
 K. Oldiges, B. R. Rad, M. Winter, *Top. Curr. Chem.* 2017, 375, 37;
 b) S. Klein, S. van Wickeren, S. Röser, P. Bärmann, K. Borzutzki,
 B. Heidrich, M. Börner, M. Winter, T. Placke, J. Kasnatscheew, *Adv. Energy Mater.* 2021, 11, 2003738.
- [46] H.-H. Ryu, N.-Y. Park, D. R. Yoon, U.-H. Kim, C. S. Yoon, Y.-K. Sun, Adv. Energy Mater. 2020, 10, 2000495.
- [47] a) H. H. Sun, H.-H. Ryu, U.-H. Kim, J. A. Weeks, A. Heller, Y.-K. Sun, C. B. Mullins, ACS Energy Lett. 2020, 5, 1136; b) H.-H. Sun, A. Manthiram, Chem. Mater. 2017, 29, 8486; c) J.-M. Kim, X. Zhang, J.-G. Zhang, A. Manthiram, Y. S. Meng, W. Xu, Mater. Today 2021, 46, 155.
- [48] Y. Duan, L. Yang, M.-J. Zhang, Z. Chen, J. Bai, K. Amine, F. Pan, F. Wang, J. Mater. Chem. A 2019, 7, 513.
- [49] H. M. Rietveld, J. Appl. Crystallogr. 1969, 2, 65.
- [50] a) M. Evertz, J. Kasnatscheew, M. Winter, S. Nowak, Anal. Bioanal. Chem. 2019, 411, 277; b) B. Vortmann-Westhoven, M. Winter, S. Nowak, J. Power Sources 2017, 346, 63.